We are IntechOpen, the world's leading publisher of Open Access books Built by scientists, for scientists

6,900
Open access books available

186,000
International authors and editors

200M
Downloads

Our authors are among the

154
Countries delivered to

TOP 1%
most cited scientists

12.2%
Contributors from top 500 universities

WEB OF SCIENCE™

Selection of our books indexed in the Book Citation Index in Web of Science™ Core Collection (BKCI)

Interested in publishing with us?
Contact book.department@intechopen.com

Numbers displayed above are based on latest data collected.
For more information visit www.intechopen.com

Chapter

Feature-Oriented Principal Component Selection (FPCS) for Delineation of the Geological Units Using the Integration of SWIR and TIR ASTER Data

Ronak Jain

Abstract

Geological studies have been performed using the Band Ratios (BR), Relative Band Depth (RBD), Mineral Indices (MI), Principal Component Analysis (PCA), Independent Component Analysis (ICA), lithological and mineral classification techniques from Short-Wave Infrared (SWIR) and Thermal Infrared (TIR) data. The chapter aims to delineate various geological units present in the area using the combination of SWIR and TIR ASTER bands through the Feature-Oriented Principal Component Selection (FPCS) technique. Different BRs and RBDs were applied to map the minerals having Al-OH and Mg-OH compounds with the chemical composition of clay (kaolinite, smectite), mica (sericite, muscovite, illite), ultramafic (lizardite, antigorite, chrysotile), talc, and carbonate (dolomite) from SWIR bands. The MI was used to map quartz-rich, mafic/ultramafic, and carbonate rocks using TIR bands. The BRs, RBDs, and MIs mapped the geological units but every single greyscale image showed a variety of features. To compile these features False Color Composite (FCC) was prepared by the combination of RBDs and MIs in the R:G:B channels which demarked various geological units to a larger extent present in the region. To overcome the limitation, the FPCS technique was applied with the integration of all BRs, RBDs, and MIs. The FPCS technique extracts valuable information from different input bands and shifts the information in the first few bands. The generated eigenvalues and eigenvectors represented the retrieved information in the specific band. The loadings of the eigenvector were used for the selection of the different brands to create the FCC for the delineation of geological strata. The best discrimination was made by the selection of FPCS1, FPCS3, and FPCS6 which differentiated all the geological units like ultramafics, dolomites, thin bands of talc, and muscovite and illite (as phyllite and mica-schist), silica-rich rocks (as quartzite), and granite outcrops.

Keywords: Remote Sensing, Optical data, Feature-Oriented Principal Component Selection, Data integration, Geological studies

1. Introduction

Water (oceans, rivers, lakes, etc.) and land (rocky mountains, hills, peneplain, islands, etc.) are the major components of the Earth's surface out of which only 29%

are occupied by the land surfaces. This 29% land coverage included the forest, desert, mountains, islands, etc. so, a very little amount of land is reserved for geological studies.

Traditional mapping methods are time-consuming and require lots of effort for the preparation of lithological maps, mineral maps, structural maps, etc. But sometimes manually collected data may have errors due to inaccessibility and recording of the data which exaggerate in due course. To avoid these errors and corrections introduced therein an advanced technology came into the picture and is known as Remote Sensing. This technique helps in the mapping of the different litho-units and associated structural features with higher accuracy in a short period as compared to the traditional methods.

Remote Sensing is a tool used for the gathering of the target information without any physical/direct contact with the earth's surface [1–6]. It is a widely used science for the identification and mapping of the various objects/materials present on the earth's crust. The electromagnetic wavelength ranges from 0.38 μm to 100 cm i.e. visible to microwave region [3] is utilized for capturing the information from the earth's surface along with different sensors to capture the EM spectrum's energy [4, 5, 7]. This technique is useful for the monitoring, protection, and management of diverse natural resources and land cover [8]. The geological studies include the demarcation of various lithologies, alteration zones, minerals, and structural features.

Multispectral Remote Sensing is utilized in the domain of geosciences for lithological mapping [9–16], mineral mapping [17–24], identification of the alteration zones related to the base metal mineralization [25–42], structural features as a controlling factor for mineralization [26, 28, 42–46] and mapping for demarcating favorable zones of mineralization [21, 47, 48]. Spectral characteristic absorption features of the rocks and minerals are utilized for the identification and mapping of lithologies and minerals like calcite, dolomite, clay, mica, and ultramafics, etc. The spectral absorption features of minerals vary with chemical composition and the resultant spectral curve varies in shape, depth, position, and asymmetry [49].

Wavelength range from 0.38 to 2.5 μm is utilized for the mapping of the various hydroxyl (Al-OH, Mg-OH), iron oxides (Fe-OH), carbonates (CO_3^{-2}), and sulphates (SO_4^{-2}) bearing minerals like clay, mica, ultramafics, hematite, limonite, dolomite, calcite, etc., due to the presence of characteristic absorption features in the VNIR and SWIR region of the EM spectrum [5, 42, 50–53]. In the case of feldspar, silica-rich rocks, and discrimination between ultramafics and dolomites are possible due to spectral features associated with the TIR region in the wavelength range of 3 to 50 μm [20, 23, 54–58]. The dissimilarities in the spectrum in the TIR spectral-domain arise due to variation in chemical composition and molecular structure.

Geological studies are done with the help of Landsat series, ASTER, Sentinel −2, SPOT, Worldview series, GeoEye, etc. optical remote sensing satellites. They are mainly utilized for the perspective of mineral exploration by using the various methods like band ratio (BR), relative band depth (RBD), Principal Component Analysis (PCA), Independent Component Analysis (ICA), Minimum Noise Fraction (MNF), unsupervised classification (K-means, isodata, etc.), supervised classification (Spectral Angle Mapper, Spectral Feature Fitting, Mixture Tuned Matched Filtering, etc.), machine learning (support vector machine, decision tree, artificial neural network, etc.). Various BR and RBD have been used for the delineation of the different rock outcrops like dolomite, calcite, Iron rich-rocks, ultramafics, epidote, clay and mica minerals, etc. [17, 21–24, 42, 58–60] and mineral prospects by the demarcation & mapping of the associated alteration zones [20, 22, 27, 28, 37, 45, 61]. Lithological mapping of the exposed outcrops and their associated features are

demarcated with the help of PCA, ICA, and MNF analyses to govern the mineral potentiality of the outcrops [9, 17, 40, 42, 44, 62, 63]. Different supervised, unsupervised, machine learning and prospectivity mapping algorithms were applied to the optical datasets to prepare the mineralogical and prospective zone maps of the region and these maps contain the information about the mineral potential zones which were utilized for the perspective of mineral explorations [17, 20, 21, 31, 42, 47, 48, 64–71].

2. Objective of the chapter

This chapter explains the use of SWIR and TIR spectral bands for the demarcation of the different minerals and lithologies present in the region. The importance of integrated datasets from SWIR and TIR-derived outcomes and the utility of the integrated dataset for the demarcation of the various litho-units has also been explained.

3. Study area and geological setup

The coverage of the study area extends between latitude 23°51′35.45″ to 24° 18′34.14″ in the North and longitude 73°28′43.95″ to 73°49′34.24″ in the East and occupies the region in Udaipur and Dungarpur districts of Rajasthan, India (**Figure 1**).

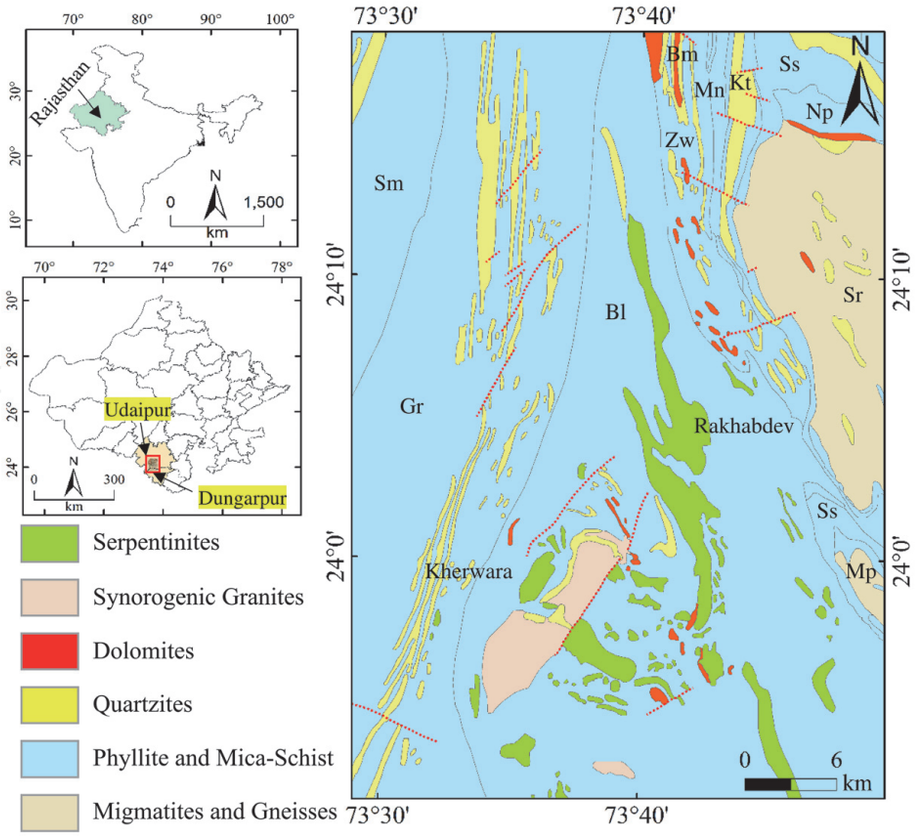

Figure 1.
Location of the study area in inset maps of India and Rajasthan. Lithological map of the study area. Modified after Gupta et al. [72]. Red dashed lines are representing the existing faults. Mp: Mando ki Pal; Sr: Sarada (BGC); Np: Natharia ki Pal; Ss: Sisa Magra; Kt: Kathalia; Mn: Mandli; Bm: Baroi Magra; Bl: Balicha; Zw: Zawar; Gr: Goran; Sm: Samlaji Formations.

Geologically the study area falls in the Udaipur sector exposes various litho-stratigraphic units of the Archean and Palaeoproterozoic age [72–74] (**Figure 1**, **Table 1**). The basement rocks are the Banded Gneissic Complex (BGC) [73, 75] or the Bhilwara Supergroup (BSG) [72, 74]. They are overlain by the rocks of the Aravalli Supergroup through an erosional unconformity. The Aravalli Supergroup has been categorized into Debari, Udaipur, Bari Lake, Jharol, Dovda, Nathdwara, Lunavada Groups [72]. It has also been subdivided into Lower, Middle, and Upper Aravalli Groups [73].

Majority of the pristine Archean features of the basement rocks have diminished due to tectono-thermal reconstruction of the basement [73]. Basement rocks from Mangalwar Complex are composed of heterogeneous rocks of amphibolite-facies metamorphites [75] or granite-greenstone belt [74]. Gneisses, metabasics, migmatites, and schists constitute the basement while greywacke, chert, marble, dolomite, quartzite, fuchsite quartzite, and mica schist represents the metasediments within the basement [74, 76]. Biotite schist, garnets, and staurolites are present in the Sarara ki Pal inlier [73, 77] and the presence of chlorite and chloritoid represents the retrogression mechanism [78].

The base of the Aravalli Supergroup is having thin bands of quartzites and pebbly oligomictic conglomerate. The continuity of quartzite is interrupted by the ESE-WNW, NE–SW, and ENE-WSW faults. In the majority of the study area phyllites and mica-schists are exposed. Graded bedded greywacke occurs within the phyllite [79]. Poddar & Mathur [80] mentioned the characteristic repetition of graded bedded and slaty phyllite. Different varieties of dolomites are exposed in the Zawar region with gradational contact with greywacke. They are pure to siliceous and massive to gritty nature. Lead-zinc mineralization is confined in the siliceous dolomites [72–75, 77, 81–86]. The lithological and chemical control of the metallogenesis in the region is supporting the concept of the syngenetic origin of lead-zinc sulphides [72]. The Rakhabdev-Dungarpur area consists of ultramafic rocks as linear belts which are serpentinized and are metasomatically altered

Era	Supergroup	Group		Formation
Paleoproterozoic	Aravalli	Synorogenic Granite and Gneiss (intrusion) Rakhabdev Ultramafic Suite (intrusion)		
		Jharol		Samlaji
				Goran
		Udaipur	Tiri Sub-group	Zawar
				Balicha/ Baroi Magra
				Mandli
		Debari		Kathalia
				Sisa Magra
				——Unconformity——
				Natharia ki Pal
				Gurali/ Basal
	——————————Unconformity——————————			
Archean	Banded Gneissic Complex	Mangalwar Complex		Mando ki Pal
				Sarada

Table 1.
Stratigraphic succession of the Aravalli Supergroup from the study area. Modified after Gupta et al. [72].

[73, 87–90]. The ultramafic rocks occur along a prominent lineament named Rakhabdev lineament which passes through the Aravalli fold belt [77, 89]. Thicker ultramafic outcrops are more massive and fractures are developed in an irregular manner [91].

4. Image processing techniques used in this investigation

4.1 Dataset

The present study uses the Advanced Spaceborne Thermal Emission and Reflection Radiometer Level-1 Precision Terrain Corrected Registered At-Sensor Radiance (ASTER L1T) dataset. ASTER sensor carries the VNIR, SWIR, and TIR scanners which have 3 (1–3), 6 (4–9), and 5 (10–14) bands respectively, and its technical specifications mentioned in **Table 2**. The ASTER L1T imagery is already geometrically corrected, georeferenced (WGS-1984) and UTM projected (UTM zone 43 N) [92].

4.2 Methodology

The overall methodology flowchart for the delineation of the various litho-units is depicted in **Figure 2**. The different litho-units were traced out with the help of the Feature-Oriented Principal Component Selection (FPCS) method which uses the various derived outcomes of band ratios, relative band depths, and mineral indices from SWIR and TIR datasets through an integrated approach.

Vegetation and water bodies are present in the region which creates a hindrance in geological mapping therefore, these land features were masked from the derived outcome. Vegetation coverage was calculated using the Normalized Difference Vegetation Index (NDVI) and the values ranging greater than 0.2 were used for the

Granule ID	Sensor-scanner	Band number	Spectral width (μm)	Spatial resolution (mtr)	Radiometric resolution	Valid range
AST_L1T_003042220 03055021_ 201504280 31510_405 83	ASTER-VNIR		0.520–0.60	15	8-bits	0–255
		2	0.630–0.690	15	8-bits	0–255
		3	0.760–0.860	15	8-bits	0–255
	ASTER-SWIR	4	1.600–1.700	30	8-bits	0–255
		5	2.145–2.185	30	8-bits	0–255
		6	2.185–2.225	30	8-bits	0–255
		7	2.235–2.285	30	8-bits	0–255
		8	2.295–2.365	30	8-bits	0–255
		9	2.360–2.430	30	8-bits	0–255
	ASTER-TIR	10	8.125–8.475	90	12-bits	0–65535
		11	8.475–8.825	90	12-bits	0–65535
		12	8.925–9.275	90	12-bits	0–65535
		13	10.25–10.95	90	12-bits	0–65535
		14	10.95–11.65	90	12-bits	0–65535

Table 2.
Technical specifications of the ASTER L1T dataset. Source: [92].

preparation of the vegetation mask. Water bodies were masked using band 1. The DN values ranging from 0 to 100 were selected to prepare the water mask. Both of the masks were applied on the derived outcomes to eliminate the vegetative lands and water bodies from the mineral and lithological map of the region.

4.2.1 Preprocessing of SWIR and TIR datasets

The ASTER SWIR dataset has the spillover of the energy from band 4 to band 5 and band 9 which is known as crosstalk effects [17, 41, 45, 47, 93, 94]. Crosstalk correction was applied for the removal of effects from the dataset and to enhances the spectral signatures of the minerals/rocks. A semi-empirical atmospheric correction, QUick Atmospheric Correction (QUAC), was applied to retrieve the surface reflection from the sensor radiance [95–100].

The ASTER TIR datasets were converted into the calibrated radiance from the digital number using Eq. (1) [46, 55, 58, 101, 102].

$$L^{i}_{sen} = cof^{i} * \left(DN^{i} - 1\right) \tag{1}$$

where:

cof^{10}	cof^{11}	cof^{12}	cof^{13}	cof^{14}
0.006882	0.006780	0.006590	0.005693	0.005224

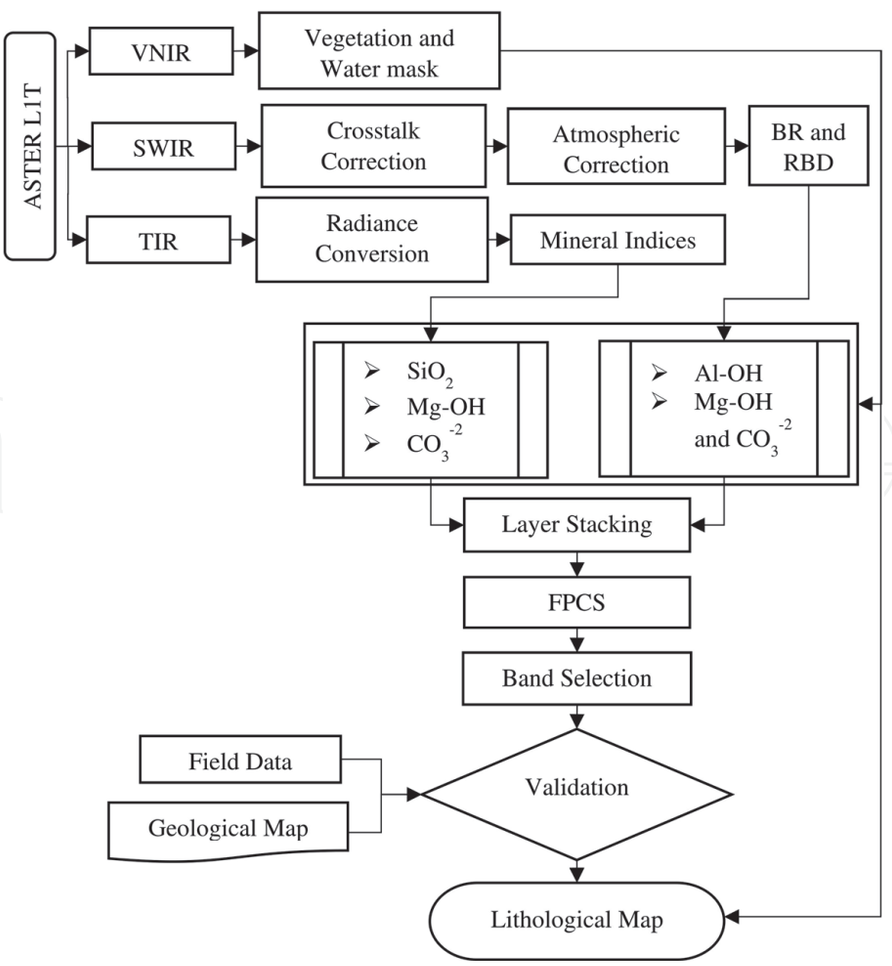

Figure 2.
Overall methodology for the derivation of the lithological map.

4.2.2 Image processing

Band Ratio (BR) is a method in which one band is divided by another band (Eq. (2)) to get the better delineation of the rocks/minerals instead of using a single band and combined with enhancement of spectral properties.

$$BR = B1/B2 \tag{2}$$

where: BR = Output Band Ratio image; B1 and B2 = Brightness value of selected bands.

Relative Band Depth (RBD) is another technique for mineral mapping in which the position and depth of the mineral spectrum were considered for calculation [103]. The RBD governs better discrimination of minerals than BR because it considers the characteristic absorption features and normalizes the effects generated due to topography and albedo [32, 37, 104]. The bands acquired the shoulder position on absorption spectrum are summed up as (S1 and S2) and divided by the band having minimal absorption value (T; Eq. (3); **Figure 3**).

$$RBD = (S1 + S2)/T \tag{3}$$

Mineral Indices (MI) is also a mathematical expression derived for mapping of the minerals by using the band math operators with different logics in the TIR wavelength region. The TIR part of the EM spectrum is utilized for the mapping of the feldspars, silicates, carbonates, and ultramafic minerals.

BR and RBD were applied on the atmospherically corrected SWIR datasets and MI was applied on the calibrated radiance TIR datasets (**Table 3**). Al-OH consisting of minerals like mica and clay minerals were delineated with the help of different BRs and RBD6 (**Table 3**). Spectral absorption minima were recorded at band 6 of ASTER at 2.205 μm which highly suitable for the mapping of clay and mica minerals [12, 34, 37, 42, 105]. Similarly, Mg-OH and CO_3^{-2} containing minerals showed the absorption minima at band 8 of ASTER at 2.336 μm which was used in the RBD8 for mapping of carbonates and ultramafics [34, 37, 106, 107]. The SiO_2 containing minerals/rocks showed the emissivity minima at the band 12 of ASTER at 9.075 μm due to vibrational energy along the Si-O bond. The CO_3^{-2} bearing minerals showed the emissivity minima at 11.318 μm which is represented by the band 14. The Mg-OH bearing minerals of ultramafics recorded the emissivity minima at band 13 at 10.657 μm.

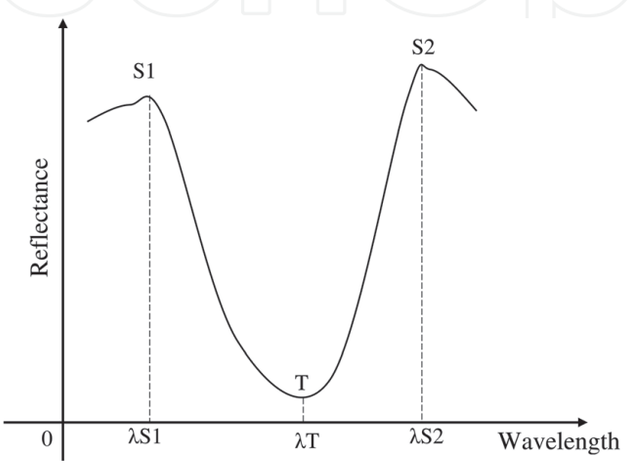

Figure 3.
Artistic sketch for interpretation of the RBD for any mineral.

Principal Component Analysis (PCA) is widely used for the identification and delineation of the litho-units and hydrothermal alteration minerals using the spectral bands generated from different sensors [9, 17, 28, 45, 48, 108]. The PCA uses the statistical mechanism for the transformation of the variables into several linear variables which are not having a correlation with each other, known as Principal Components (PCs). It is implemented on the symmetric matrix which is based on the either correlation matrix or covariance matrix (Eq. (4)). The PCs have the information related to the specific mineral which can be retrieved with the help of loadings of eigenvector (Eq. (5)). The strong eigenvector loadings of the PCs were utilized for the demarcation of the various mineral/groups through its PC indicative bands (Eq. (6)) which showed bright and dark pixels for the specific minerals in the PC image [108]. The present work uses the Feature-Oriented Principal Component Selection (FPCS) on the integrated data derived from BR, RBD, and MI from the ASTER SWIR and TIR data for mapping of the lithological units present in the region. The FPCS was used to achieve the desired goal by the combination of SWIR and TIR-derived outcomes. The phyllite and mica-schist can be marked with the help of BRs and RBD6, carbonates and ultramafics gave a similar tone by the use of RBD8 of SWIR region while MI has the capabilities to distinguish these two minerals/groups. Quartzites were not mapped in the SWIR EM region due to lack of the characteristic absorption band while TIR EM regions have these capabilities. Mineral/rock identification was not possible through the single kind of dataset like only by SWIR only by TIR so, integrated approach was required to delineate all lithological units existed in the study area. Therefore, FPCS was implemented on the basis of covariance matrix of the integrated outcomes of ASTER SWIR and TIR. The derived eigenvector matrix is tabulated in **Table 4**.

$$cov(X,Y) = \frac{1}{n-1}\sum_{i=1}^{n}(Xi - \bar{x})\,(Yi - \bar{y}) \tag{4}$$

S. no.	Mineral composition	Indicator minerals	Formula	Absorption band: wavelength (μm)	References
SWIR bands Band Ratio (BR)					
1.	Al-OH	Sericite, smectite, muscovite, and illite	B7/B6	6: 2.205	[106]
2.			B4/B6		[8]
3.		Alunite and kaolinite	B7/B5	5: 2.167	[106]
Relative Band Depth (RBD)					
4.	Al-OH (RBD6)	Sericite, smectite, and illite	(B5 + B8) /B6	6: 2.205	[12, 42]
5.	Mg-OH and CO_3^{-2} (RBD8)	Carbonates and ultramafics	(B6 + B9) /B8	8: 2.336	[37, 106]
TIR bands Mineral Indices (MI)					
6.	Mg-OH	Ultramafics	(B12/B13) × (B14/B13)	13: 10.657	[23]
7.	SiO_2	Silica-rich	(B11/ (B10 + B12)) × (B13/B12)	12: 9.075	[56]
8.	CO_{3-2}	Carbonates	B13/B14	14: 11.318	[54, 101]

Table 3.
BR, RBD, and MI used for the derivation of the mineral maps from ASTER SWIR and TIR bands.

Eigenvectors	MI CO_3^{-2}	MI SiO_2	MI Mg-OH	BR 7/5	RBD6	RBD8	BR 4/6	BR 7/6
Band 1	0.006692	−0.02224	0.056749	−0.18058	−0.50483	0.772556	−0.11678	−0.31352
Band 2	−0.02898	−0.01231	−0.04299	−0.08242	−0.4053	−0.48972	−0.72584	−0.24381
Band 3	−0.69819	−0.33987	−0.62711	−0.0019	0.001132	0.049081	0.036474	0.002323
Band 4	−0.006	−0.01368	0.020563	−0.26053	−0.48361	−0.39945	0.669243	−0.30025
Band 5	0.015369	0.017849	−0.02398	0.807885	−0.49943	−0.00099	0.088098	0.298333
Band 6	−0.0354	−0.00343	0.042673	−0.48543	−0.31084	0.003489	−0.04809	0.813837
Band 7	0.216406	0.736543	−0.6363	−0.05878	−0.02868	0.036048	0.014719	0.000581
Band 8	0.680651	−0.58381	−0.44041	−0.03078	−0.01117	0.007118	0.004385	0.027843

Table 4.
Eigenvector matrix generated from the integrated derived mineral maps for FPCS.

$$A\vec{v} = \lambda\vec{v} \text{ or } \vec{v}(A - \lambda I) = 0 \quad (5)$$

$$y = W' \times x \quad (6)$$

where:
cov(X, Y) = Covariance matrix; X and Y = Variables;
$A\vec{v}$ = eigenvector of matrix A; λ = eigenvalue (scaler value); I = Identity matrix.
y = Final outcome; W′ = transpose of scaler data; x = Feature vector.

5. Results

5.1 Band ratios (BRs) and relative band depths (RBDs)

5.1.1 Distribution of Al-OH consisting minerals

Clay (kaolinite, illite, montmorillonite) and mica (sericite and muscovite) minerals consist of the Al-OH in their chemical composition. These minerals especially illite, montmorillonite, muscovite, and sericite exhibited characteristic spectral absorption features at a wavelength of 2.205 μm which is detectable with band 6 (2.185–2.225 μm) of the ASTER sensor. Kaolinite mineral also showed minor absorption at 2.165 μm for that band 5 (2.145–2.185 μm). The Al-OH consisting of minerals were mapped in the quartzites south of Rakhabdev and near the granitic outcrop of Kherwara inlier [89]. Phyllite and mica-schist also depicted higher values for Al-OH containing minerals by using BR 7/6 (**Figure 4A**). The granitoids of the basement, granites, and quartzites have high values for Al-OH by using BR 4/6 (**Figure 4B**). On applying BR 7/5, almost the entire region depicted higher values for kaolinite (Al-OH) which is indicative of a poor interpretation (**Figure 4C**). The RBD (5 + 8)/6 gave a similar kind of result like BR 7/6. It depicted higher values of the Al-OH consisting of rocks/minerals for the quartzites, phyllites, mica-schists, conglomerate, and arkose litho-units (**Figure 4D**). Ultramafics and carbonates (dolomite) have very low values from BRs 7/6, 4/5, and RBD6 due to the absence of Al-OH minerals.

5.1.2 Distribution of Mg-OH and CO_{3-2} consisting minerals

Ultramafics are having the Mg-OH while dolomites are having both Mg-OH and CO_{3-2} constituents in their composition. These minerals have the characteristic absorption feature at 2.33 μm, which occurs at band 8 (2.295–2.365 μm). The RBD (6 + 9)/8 was applied for mapping of the Mg-OH and CO_{3-2} consisting of minerals. Ultramafics depicted extremely high values while dolomites have moderate values (**Figure 5A**). The regions of Zawarmala and Hati Magra are dominated by dolomite exposures but a poor carbonate map as an outcome may be due to the presence of extreme vegetation on the hills.

A lithological map has also been prepared from RBD6, RBD8, and BR4/6 in RGB channels respectively (**Figure 5B**). Basement rocks are depicted as pinkish-blue, phyllite, and mica-schist as reddish color. Dolomite is depicted as dark green while ultramafics are as green color. Quartzites are light pink in color. The resultant map discriminates the various lithologies present in the area and is comparable with the published geological maps.

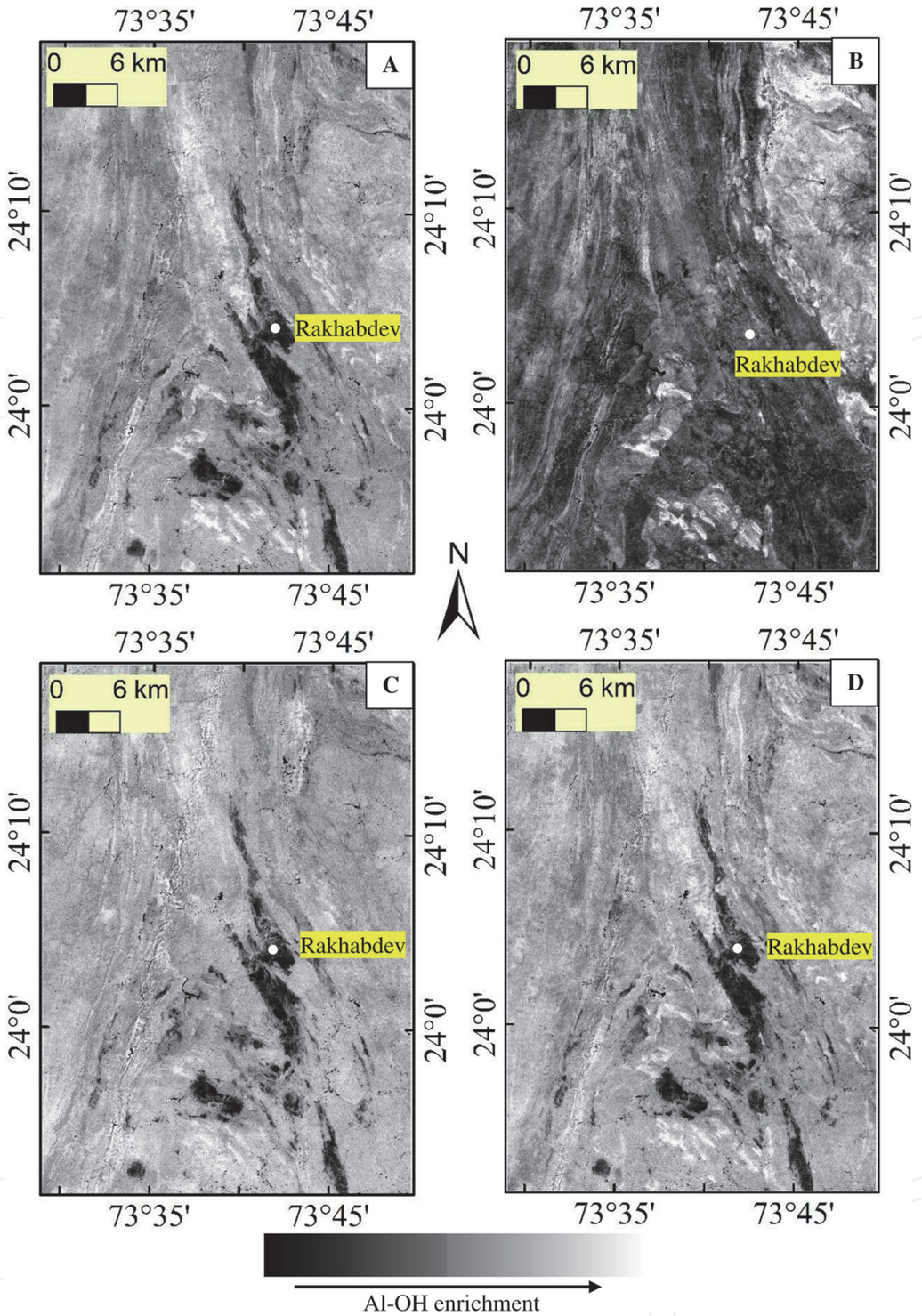

Figure 4.
Results from the SWIR data for Al-OH bearing minerals using the techniques of BRs and RBDs. (A) BR 7/6 for mica and clay minerals. (B) BR 4/6 for clay minerals. (C) BR 7/5 for kaolinite. (D) RBD6 (5 + 8)/6 for clay and mica minerals.

5.2 Mineral indices (MI)

5.2.1 Distribution of mafics/ultramafics

The ultramafic map was developed using the mafic index defined by Guha & Vinod Kumar [23]. The derived map of the mafic index mapped the outcrops of the ultramafics with very higher values near the Rakhabdev region and along other thin

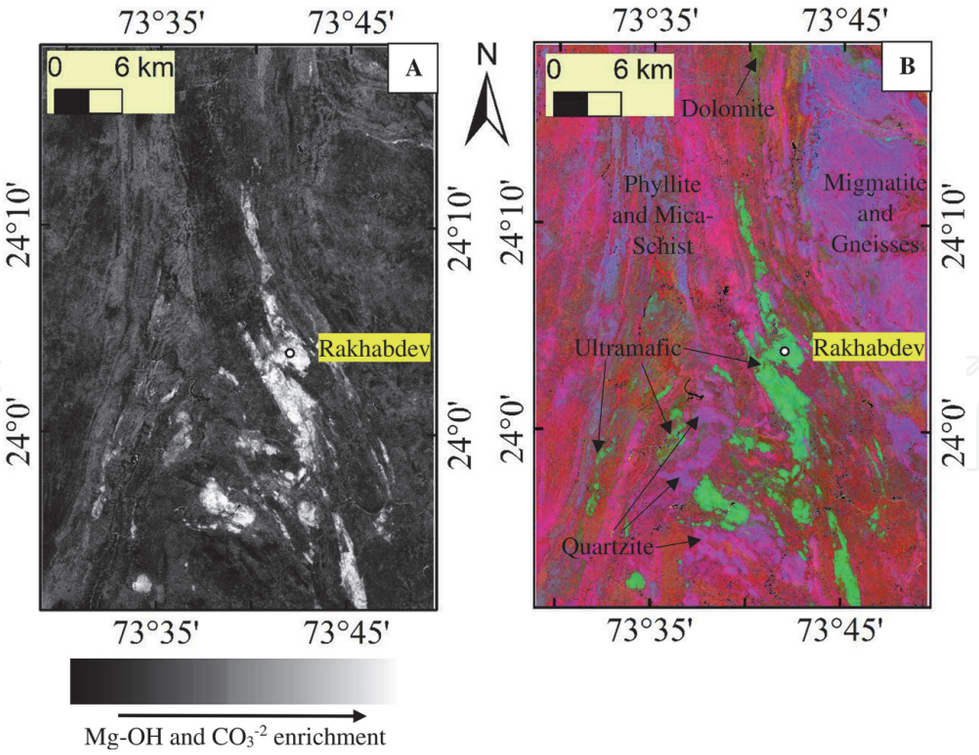

Figure 5.
Results from the SWIR data. (A) RBD8 (6 + 9)/8 for the mapping of ultramafics and carbonates. (B) Lithological map using the RBD6, RBD8, and BR4/6 in the RGB channels.

belts of the ultramafic outcrops south of Rakhabdev and on the west of Kherwara (**Figure 6A**). The dolomites were suppressed and showed their uniqueness to distinguish by ultramafics.

5.2.2 Distribution of SiO_2 consisting minerals

Silica-rich rocks were marked by using the silica index of Rockwell & Hofstra [56] (**Figure 6B**). Quartzites present on the outer periphery of basement rocks were precisely demarcated through the silica index. Silica index also mapped the quartzites present adjacent to the dolomites in the Zawar region. The derived mineral map showed very low values for the ultramafics and dolomites.

5.2.3 Distribution of CO_{3-2} consisting minerals

Ninomiya et al. [54] defined the mathematical expression for the mapping of carbonate rocks and the derived mineral map showed dense noise, consequently, identification of the carbonate outcrops was not precisely obtained (**Figure 6C**). The presence of stripping noise and poor signal at band 14 hinders the demarcation of carbonate outcrops [20, 109, 110]. The ultramafics and quartzitic outcrops were depicting very low values in the carbonate map.

A lithological map was prepared using the silica, mafic, and carbonate indices in RGB channels respectively (**Figure 6D**). Dolomites of the region were marked by bluish-green color but the majority of the region was marked as bluish-green color which is a poor identification for dolomites, quartzites are depicting the maroon color and ultramafics as bright green color. The yellow color at the tips of ultramafics and within the massive outcrops of ultramafics are identified as talc.

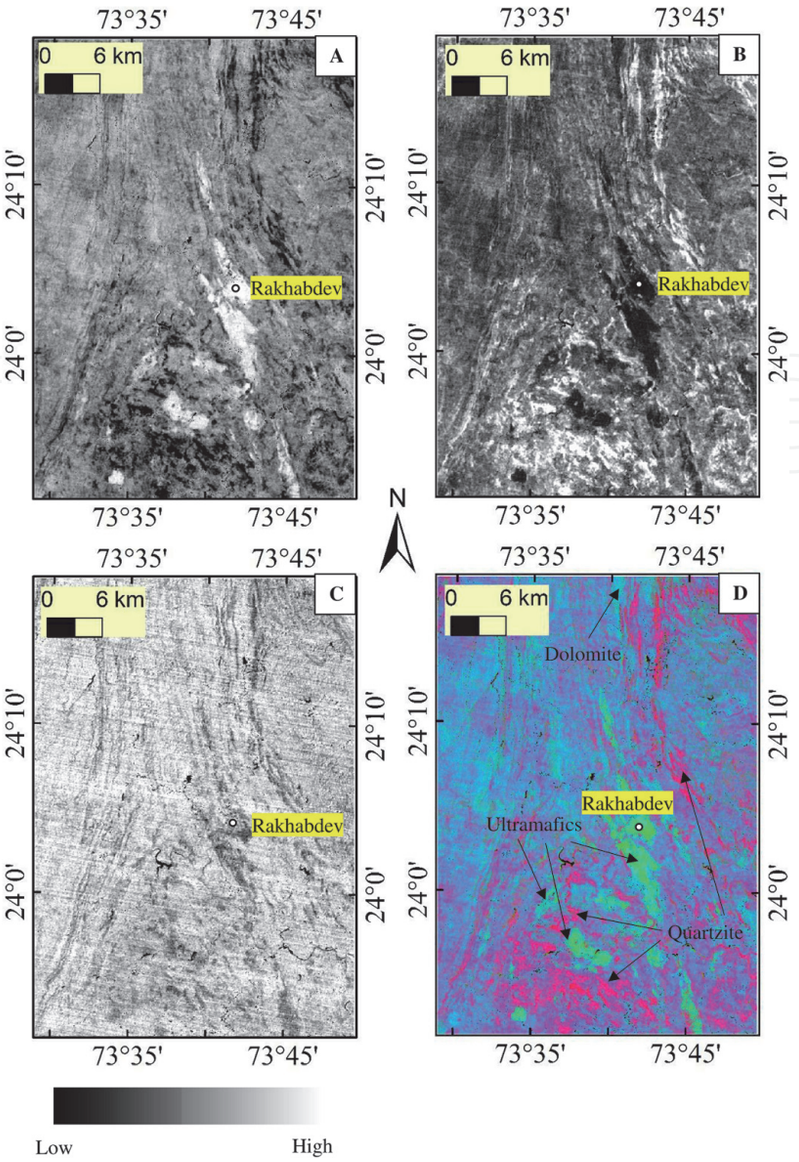

Figure 6.
Results derived from the TIR data. (A) Ultramafic map derived using the Guha and Vinod Kumar index [23]. (B) Silica-rich rocks were demarcated by using the Rockwell and Hofstra index [56]. (C) Carbonate map derived using Ninomiya et al. index [54]. (D) Lithological map prepared using the silica-rich, ultramafics, and carbonate maps in RGB channels.

5.3 Feature-oriented principal component selection (FPCS)

The FPCS technique was implemented to the integrated derived outcomes from BRs, RBDs, and MIs of the ASTER SWIR and TIR bands for discrimination of the different litho-units present in the study area. The generated eigenvector matrix from the FPCS from the integrated derived mineral maps is shown in **Table 4**. The PC1 shows the extreme values for the ultramafics and moderate values for the dolomites. Quartzites showed very low values and represented dark pixels (**Figure 7**). The PC1 shows the combined outcome from the RBD8 and MI Mg-OH because RBD8 highlighted ultramafics and dolomites of the region while MI Mg-OH mapped the ultramafics and suppressed the quartzites of the region. The PC2 showed extremely high values for phyllite and mica-schists and dark pixels for the quartzites of the region. The ultramafics & dolomites of the region are depicting the low values (**Figure 7**). The PC2 showed the combination of BR 4/6, BR 7/5, and RBD6 in which BR 4/6 highlighted the silica-rich rocks. The Al-OH consisting minerals are suppressed in the PC2 while RBD6 highlighted the phyllite and

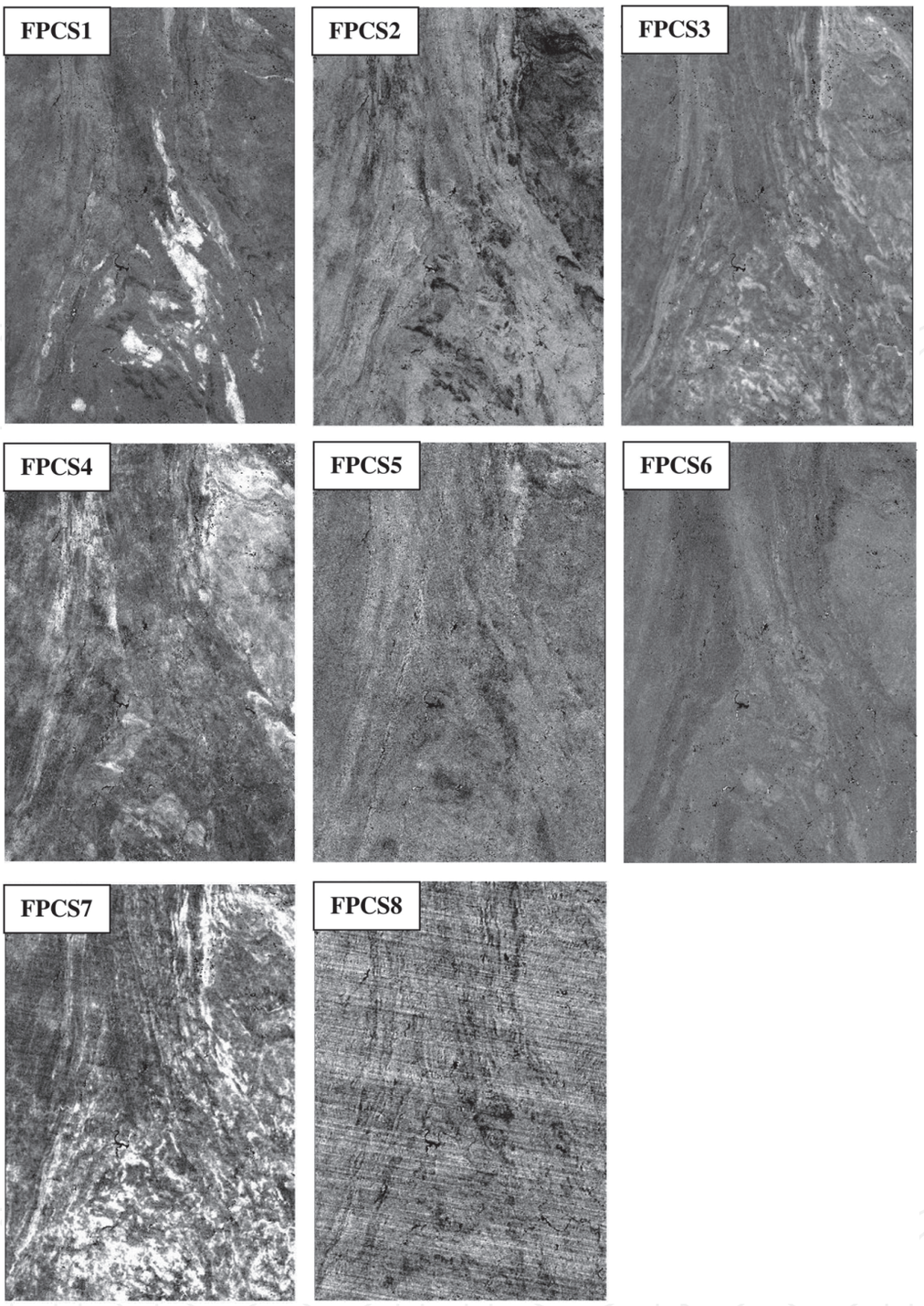

Figure 7.
FPCS components generated using the PCA technique on integrated BRs, RBDs, and MIs from the SWIR and TIR bands.

mica-schists as Al-OH consisting rocks and BR 7/5 also highlighted the Al-OH consisting minerals. The PC3 depicted very high values for quartzites i.e. silica-rich rocks as by MI SiO_2 but on the south of Rakhabdev the distribution of silica-rich rocks is not showing the vague distribution like MI SiO_2, and a clear delineation of quartzites are obtained (**Figure 7**). The PC4 depicted a similar kind of pattern as BR 4/6 but the extremity of the pixel values gets lower down and appearance gets noisy (**Figure 7**). The PC6 depicted higher values for the ultramafics and silica enriched rocks of the granitoids & migmatites from the basement, quartzites, and phyllite, and mica-schist while carbonates are depicted moderate values (**Figure 7**). The PC6 is helpful for the delineation of the litho-units of the region but the band showed an

association of the moderate amount of noise. The PC5, PC7, and PC8 are not useful for the discrimination of the geological units due to the presence of a high amount of noise with them (**Figure 7**).

FCC was been prepared using the combinations of bands PC1, PC3, and PC6 respectively for delineation of different litho-units (**Figure 8**). Granitoids and migmatites appeared as greenish-blue colors while quartzites as light green with a mixture of cyan color. Phyllite and mica-schist appeared as dark blue to greenish-brown color. Conglomerate and meta-arkose gave shades of green color. Dolomites appeared as purplish colors and ultramafics as pinkish colors. Light yellow color on the tips of ultramafics and within the ultramafics which showed the presence of talc.

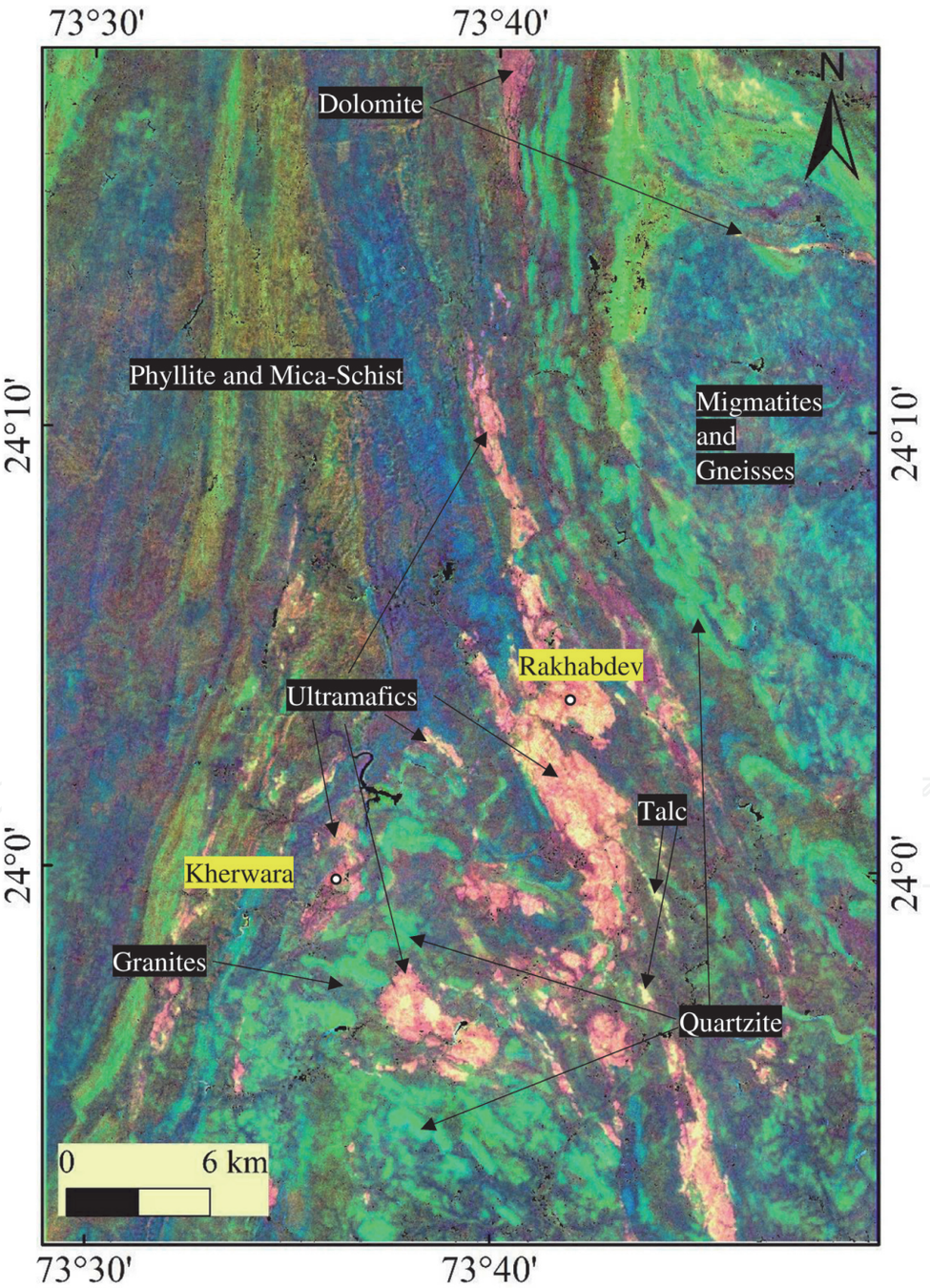

Figure 8.
Lithological map of the study area prepared by the combination of FPCS1, FPCS3, and FPCS6 in the RGB channels respectively.

5.4 Verification of the derived lithological map

To verify the different litho-units of the region various field reconnaissance was conducted and for the estimation of the overall accuracy of the generated lithological map, GPS surveys were carried out. Various traverses were conducted along the major litho-units of the region and some traverses were conducted for the verification of changes observed in the generated lithological map. Field photographs and rock samples were collected for the determination of accurate locations and associated lithology/ies if present at the contact zone. Pink colored granites from the Kherwara Inlier were observed (**Figure 9A**) and deformed quartzites were present with the contact of it (**Figure 9B**). Serpentinites of the Rakhabdev showed the variation all along the belt-like massive to fibrous nature and open mining pits of the serpentinites in the massive variants (**Figure 9C**, **D**, **G** and **I**). In the field, outcrops of the different dolomites were observed (**Figure 9E**) associated with the quartzites, metagraywacke, phyllite, and mica-schist (**Figure 9F**). Contact between the phyllite & mica-schist and quartzites was also observed (**Figure 9H**). Talc was also observed in the field and it is mainly in the region of deformation (**Figure 9G**). The isolated patch of the serpentinite near the Parbeela region shows the contact with the granites of Kherwara Inlier. Furthermore, the accuracy assessment was carried out between the generated lithological map and field-collected information

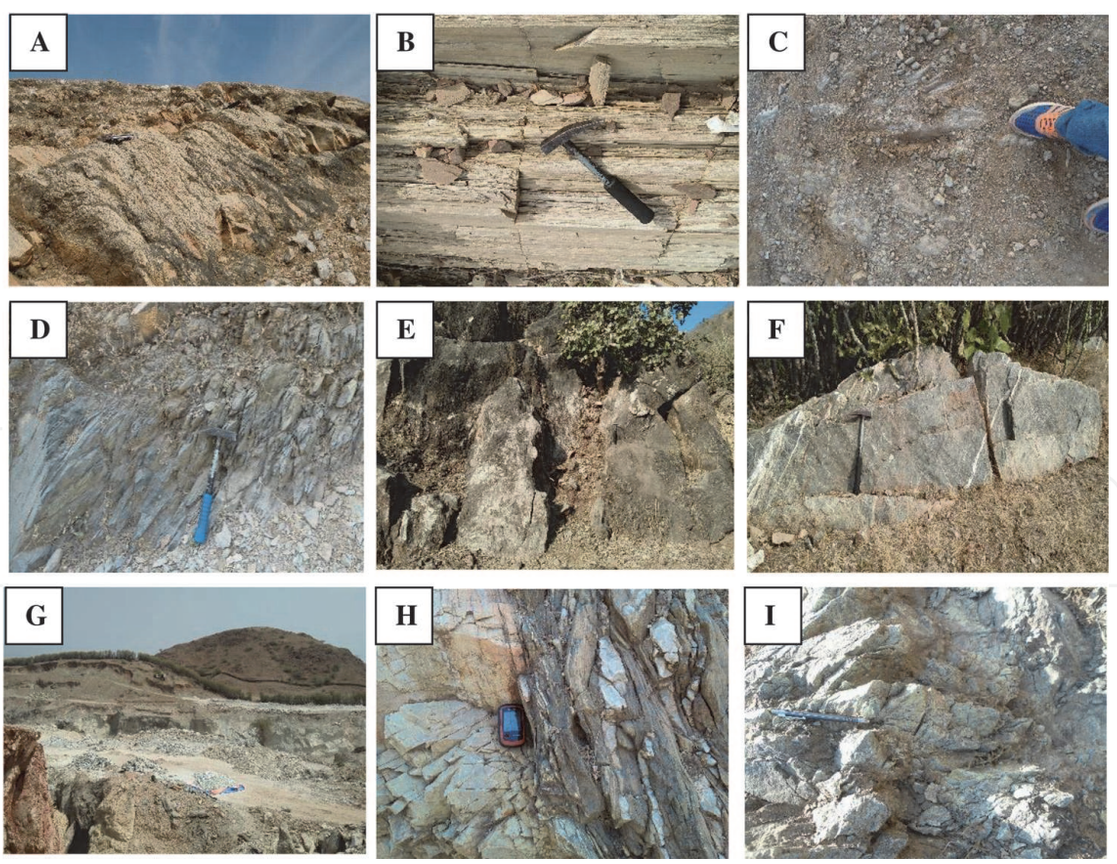

Figure 9.
Field validation of the different litho-units. (A) Granites from the Kherwara inlier. (B) Mullions of quartzites from Kherwara inlier. (C) Talc mineralization along the serpentinites from southeast of Rakhabdev. (D) Massive serpentinites from Rakhabdev. (E) Dolomites from the northeast of Rakhabdev. (F) Massive quartzites from the east of Rakhabdev. (G) Mining activities for talc from the hinges of serpentinites outcrops from south of Rakhabdev. (H) Contact between the quartzites and phyllites from north of Rakhabdev. (I) Serpetninites and its alteration products from south of Rakhabdev.

Class	Dolomite	Serpentinite	Quartzite	Talc	Phyllite	Granite	User's Accuracy
Dolomite	34	1	0	2	0	1	89.47%
Serpentinite	2	16	0	1	0	0	84.21%
Quartzite	0	1	10	0	2	0	76.92%
Talc	2	1	0	14	1	0	77.78%
Phyllite	1	0	2	0	17	1	80.95%
Granite	0	0	0	0	0	13	100.00%
Producer's Accuracy	87.18%	84.21%	83.33%	82.35%	85.00%	86.67%	
			Overall Accuracy				85.25%
			Kappa Coefficient				0.8164

Table 5.
Accuracy assessment of the derived lithological map using the GPS survey collected localities.

using the GPS (**Table 5**). The derived confusion matrix shows the overall accuracy and kappa coefficient as 85.25% and 0.8164 respectively for the lithological map.

6. Discussions

The study area belongs to the Aravalli Orogeny and several deformational histories were recorded [72–75, 77, 81, 84–86, 89, 111–113]. The remote sensing technique is widely used for mineral mapping and lithological mapping around the study area [9, 58, 102, 114]. In the present research, different BR, RBD, & MI and their combinations were generated using the ASTER SWIR and TIR bands for the demarcation of the different litho-units present in the region. The BRs and RBDs were used to derive the Al-OH and Mg-OH & CO_{3-2} consisting minerals [8, 12, 35, 37, 42, 106] like phyllite & mica-schist, carbonates, and ultramafics. And their FCC combinations helped to delineate granitoids, granites, phyllite, mica-schist, quartzites, dolomite, and ultramafics (**Figure 5B**). The MIs were used to derive SiO2, Mg-OH, and CO_{3-2} mineral maps of the region [23, 54–56, 58, 101], and quartzites, ultramafics, and carbonates were delineated. The FCC also helped a lot to determine the lithologies of the region but were limited to the quartzites, ultramafics, and carbonates (**Figure 6D**).

FPCS technique was utilized for the delineation of litho-units present in the region on the basis of the combined results derived from the BRs, RBDs, and MIs from the ASTER SWIR and TIR bands. The PC1, PC3, and PC6 have capabilities to discriminate the ultramafics, carbonates, quartzites, phyllite, mica-schist, and granitoids. The prepared FCC using the combinations of these PCs demarcated the granitoids, granites, phyllite, mica-schist, quartzites, conglomerate, meta-arkose, dolomites, ultramafics (**Figure 8**). The integrated approach from the ASTER SWIR and TIR proved its potentials for lithological mapping. The generated confusion matrix showed the overall accuracy as 85.25% and kappa coefficient as 0.8164 in which maximum producer's accuracy (%) was attained by dolomite while user's accuracy (%) by granite. Field validation was performed on the generated lithological map by observing the various litho-units present on the surficial exposures and gathered the location information by the use of a GPS survey. Association of quartzites with dolomites and serpentinites with dolomites was observed in the

field. Talc is found with the serpentinites and was produced due to the process of serpentinization and mainly formed at the deformational zones [115].

7. Conclusions

1. Lithological and mineral mapping of the region can be done with the help of various BR, RBD, & MI and by the combinations of these but discrimination between every single litho-unit is not possible with it.

2. The data integration (combination of derived mineral maps from ASTER SWIR and TIR bands) approach played an important role to obtain the desired research goal.

3. PCA is a statistical technique that is utilized for the demarcation of the various litho-units using the original bands but, in this research, FPCS was utilized on the integrated data which shows its capabilities towards discrimination of every single litho-unit.

4. PC1, PC3, and PC6 from the FPCS were utilized for the discrimination of various litho-units in which talc is also identified within ultramafics which is an alteration product of serpentinization.

5. The overall accuracy and kappa coefficient of the generated lithological map are 85.25% and 0.8164 respectively and calculated with the help of GPS surveys.

Acknowledgements

The author is thankful to USGS Earth Explorer to provide the ASTER dataset under the open distribution policy. Thanks to the Heads of the Department of Geology for providing the necessary facilities for conducting the research. Some part of this chapter has been taken from the Ph.D. thesis of the author.

Conflict of interest

The author declares no conflict of interest.

IntechOpen

Author details

Ronak Jain[1,2]

1 Department of Remote Sensing, School of Earth Sciences, Banasthali Vidyapith, Banasthali, India

2 Department of Geology, Faculty of Earth Sciences, Mohanlal Sukhadia University, Udaipur, India

*Address all correspondence to: jainronak75@yahoo.in

IntechOpen

© 2021 The Author(s). Licensee IntechOpen. This chapter is distributed under the terms of the Creative Commons Attribution License (http://creativecommons.org/licenses/by/3.0), which permits unrestricted use, distribution, and reproduction in any medium, provided the original work is properly cited. CC BY

References

[1] Pandey SN. Principles and Applications of Photogeology. 1st ed. United States: John Wiley and Sons Ltd; 1984. 1-382 p.

[2] Guha PK. Remote Sensing for the Beginner. New Delhi, India: East-West Press Ltd.; 2003. 129 p.

[3] Gupta RP. Introduction. In: Remote Sensing Geology. 2nd ed. New York: Springer- Verlag Berlin Heidelberg GmbH; 2003. p. 1–16.

[4] Jain R, Kumar A, Sharma RU. Study of Mineral Mapping Techniques using Airborne Hyperspectral Data: Exploring the potential of AVIRIS-NG for Mineral Identification. Germany: Lap Lambert Academic Publishing; 2018. 1-72 p.

[5] Jain R, Sharma RU. Airborne hyperspectral data for mineral mapping in Southeastern Rajasthan, India. Int J Appl Earth Obs Geoinf. 2019;81:137–145.

[6] Jensen JR. Introductory Digital Image Processing: A Remote Sensing Perspective. 4th ed. Pearson Education, Inc; 2015. 623 p.

[7] Jain R, Kumar A, Sharma RU. Study of Mineral Mapping Techniques: A case study in Southeastern Rajasthan. In: Proceedings of 38th Asian Conference on Remote Sensing- Space Applications: Touching Human Lives, ACRS. New Delhi, India: Curran Associates, Inc., New York; 2017. p. 2799–807.

[8] Sabins FF. Remote Sensing: Principles and Interpretation. 3rd ed. United States of America: Waveland Press, Inc.; 2007. 1-485 p.

[9] Kumar C, Shetty A, Raval S, Sharma R, Ray PKC. Lithological Discrimination and Mapping using ASTER SWIR Data in the Udaipur area of Rajasthan, India. Procedia Earth Planet Sci. 2015;11:180–188.

[10] Ninomiya Y. Toward Lithological Mapping of Arabian Peninsula Using ASTER Multispectral Thermal Infrared Data. In: El-Askary H, Lee S, Heggy E, Pradhan B, editors. Advances in Remote Sensing and Geo Informatics Applications CAJG 2018 Advances in Science, Technology & Innovation (IEREK Interdisciplinary Series for Sustainable Development). Springer, Cham; 2019. p. 181–184.

[11] Ninomiya Y, Fu B. Wide area lithologic mapping with ASTER thermal infrared data: Case studies for the regions in/around the Pamir Mountains and the Tarim basin. IOP Conf Ser Earth Environ Sci. 2017;74(1):1–4.

[12] Rowan LC, Mars JC, Simpson CJ. Lithologic mapping of the Mordor, NT, Australia ultramafic complex by using the Advanced Spaceborne Thermal Emission and Reflection Radiometer (ASTER). Remote Sens Environ. 2005; 99(1–2):105–126.

[13] Vincheh ZH, Arfania R. Lithological Mapping from OLI and ASTER Multispectral Data Using Matched Filtering and Spectral Analogues Techniques in the Pasab-e-Bala Area, Central Iran. Open J Geol [Internet]. 2017;7:1494–508. Available from: http://www.scirp.org/journal/ojg

[14] Ozkan M, Celik O, Ozyavas A. Lithological discrimination of accretionary complex (Sivas, northern Turkey) using novel hybrid color composites and field data. J African Earth Sci. 2018;138:75–85.

[15] Madani AA, Emam AA. SWIR ASTER band ratios for lithological mapping and mineral exploration: a case study from El Hudi area, southeastern desert, Egypt. Arab J Geosci. 2011;4(1–2):45–52.

[16] Askari G, Pour A, Pradhan B, Sarfi M, Nazemnejad F. Band Ratios

Matrix Transformation (BRMT): A Sedimentary Lithology Mapping Approach Using ASTER Satellite Sensor. Sensors. 2018;18(10):3213.

[17] Pour AB, Hashim M. The application of ASTER remote sensing data to porphyry copper and epithermal gold deposits. Ore Geol Rev. 2012;44: 1–9.

[18] Pal SK, Majumdar TJ, Bhattacharya AK, Bhattacharyya R. Utilization of Landsat ETM+ data for mineral-occurrences mapping over Dalma and Dhanjori, Jharkhand, India: an Advanced Spectral Analysis approach. Int J Remote Sens. 2011;32 (14):4023–4040.

[19] Zhang X, Pazner M, Duke N. Lithologic and mineral information extraction for gold exploration using ASTER data in the south Chocolate Mountains (California). ISPRS J Photogramm Remote Sens. 2007;62(4): 271–282.

[20] Guha A, Yamaguchi Y, Chatterjee S, Rani K, Vinod Kumar K. Emittance Spectroscopy and Broadband Thermal Remote Sensing Applied to Phosphorite and Its Utility in Geoexploration: A Study in the Parts of Rajasthan, India. Remote Sens. 2019;11(9):1003.

[21] Rani K, Guha A, Mondal S, Pal SK, Vinod Kumar K. ASTER multispectral bands, ground magnetic data, ground spectroscopy and space-based EIGEN6C4 gravity data model for identifying potential zones for gold sulphide mineralization in Bhukia, Rajasthan, India. J Appl Geophys. 2019; 160:28–46.

[22] Guha A, Singh VK, Parveen R, Vinod Kumar K, Jeyaseelan, A. T. Dhanamjaya Rao EN. Analysis of ASTER data for mapping bauxite rich pockets within high altitude lateritic bauxite, Jharkhand, India. Int J Appl Earth Obs Geoinf. 2013;21:184–194.

[23] Guha A, Vinod Kumar K. New ASTER derived thermal indices to delineate mineralogy of different granitoids of an Archaean Craton and analysis of their potentials with reference to Ninomiya's indices for delineating quartz and mafic minerals of granitoids—An analysis in Dharwar Craton. Ore Geol Rev. 2016;74:76–87.

[24] Guha A, Vinod Kumar K, Dhananjaya Rao EN, Parveen R. An image processing approach for converging ASTER-derived spectral maps for mapping Kolhan limestone, Jharkhand, India. Curr Sci. 2014;106(1): 40–49.

[25] Yajima T, Yamamoto K, Yamamoto K, Hayashi T. Identification of hydrothermal alteration zones for exploration of porphyry copper deposits using ASTER data. J Remote Sens Soc Japan. 2007;27(2):117–128.

[26] Pour AB, Hashim M. Hydrothermal alteration mapping from Landsat-8 data, Sar Cheshmeh copper mining district, south-eastern Islamic Republic of Iran. J Taibah Univ Sci [Internet]. 2015;9(2):155–166. Available from: h ttp://dx.doi.org/10.1016/j.jtusc i.2014.11.008

[27] Pour AB, Hashim M, Hong JK, Park Y. Lithological and alteration mineral mapping in poorly exposed lithologies using Landsat-8 and ASTER satellite data: North-eastern Graham Land, Antarctic Peninsula. Ore Geol Rev. 2019;108:112–133.

[28] Sekandari M, Masoumi I, Pour AB, Muslim AM, Hossain MS, Misra A. ASTER and WorldView-3 satellite data for mapping lithology and alteration minerals associated with Pb-Zn mineralization. Geocarto Int. 2020;1–31.

[29] Abdelsalam MG, Stern RJ, Berhane WG. Mapping gossans in arid regions with Landsat TM and SIR-C images: The Beddaho Alteration Zone in

northern Eritrea. J African Earth Sci. 2000;30(4):903–916.

[30] Khaleghi M, Ranjbar H. Alteration Mapping for Exploration of Porphyry Copper Mineralization in the Sarduiyeh Area, Kerman Province, Iran, Using ASTER SWIR Data. Aust J Basic Appl Sci. 2011;5(8):61–69.

[31] Honarmand M. Application of Airborne Geophysical and ASTER Data for Hydrothermal Alteration Mapping in the Sar-Kuh Porphyry Copper Area, Kerman Province, Iran. Open J Geol [Internet]. 2016;6:1257–1268. Available from: http://www.scirp.org/journal/ojg

[32] Yan J, Zhou K, Liu D, Wang J, Wang L, Liu H. Alteration information extraction using improved relative absorption band-depth images, from HJ-1A HSI data: a case study in Xinjiang Hatu gold ore district. Int J Remote Sens. 2014;35(18):6728–6741.

[33] Honarmand M, Ranjbar H, Shahabpour J. Application of Principal Component Analysis and Spectral Angle Mapper in the Mapping of Hydrothermal Alteration in the Jebal–Barez Area, Southeastern Iran. Resour Geol. 2012;62(2):119–139.

[34] Zhang T, Yi G, Li H, Wang Z, Tang J, Zhong K, et al. Integrating Data of ASTER and Landsat-8 OLI (AO) for Hydrothermal Alteration Mineral Mapping in Duolong Porphyry Cu-Au Deposit, Tibetan Plateau, China. Remote Sens. 2016;8(11):890.

[35] Parashar C. Mapping of Alteration mineral zones by combining techniques of Remote Sensing and Spectroscopy in the parts of SE-Rajasthan. Andra University, Visakhapatnam; 2015.

[36] Moghtaderi A, Moore F, Mohammadzadeh A. The application of advanced space-borne thermal emission and reflection (ASTER) radiometer data in the detection of alteration in the Chadormalu paleocrater, Bafq region, Central Iran. J Asian Earth Sci. 2007;30 (2):238–252.

[37] Sengar VK, Venkatesh AS, Champati Ray PK, Sahoo PR, Khan I, Chattoraj SL. Spaceborne mapping of hydrothermal alteration zones associated with the Mundiyawas-Khera copper deposit, Rajasthan, India, using SWIR bands of ASTER: Implications for exploration targeting. Ore Geol Rev. 2020;118:103327.

[38] Tommaso ID, Rubinstein N. Hydrothermal alteration mapping using ASTER data in the Infiernillo porphyry deposit, Argentina. Ore Geol Rev. 2007; 32(1–2):275–290.

[39] Lampinen HM, Laukamp C, Occhipinti SA, Metelka V, Spinks SC. Delineating Alteration Footprints from Field and ASTER SWIR Spectra, Geochemistry, and Gamma-Ray Spectrometry above Regolith-Covered Base Metal Deposits - An Example from Abra, Western Australia. Econ Geol. 2017;112(8):1977–2003.

[40] Pour AB, Hashim M. Spectral transformation of ASTER data and the discrimination of hydrothermal alteration minerals in a semi-arid region, SE Iran. Int J Phys Sci. 2011;6(8):2037–2059.

[41] Pour AB, Hashim M. Identification of hydrothermal alteration minerals for exploring of porphyry copper deposit using ASTER data, SE Iran. J Asian Earth Sci. 2011;42(6):1309–1323.

[42] Van der Meer FD, Van der Werff HMA, Van Ruitenbeek FJA, Hecker CA, Bakker WH, Noomen MF, et al. Multi- and hyperspectral geologic remote sensing: A review. Int J Appl Earth Obs Geoinf [Internet]. 2012;14(1): 112–128. Available from: http://dx.doi.org/10.1016/j.jag.2011.08.002

[43] Amri K, Mahdjoub Y, Guergour L. Use of Landsat 7 ETM+ for lithological

and structural mapping of Wadi Afara Heouine area (Tahifet–Central Hoggar, Algeria). Arab J Geosci. 2011;4(7–8): 1273–1287.

[44] Al-Nahmi F, Saddiqi O, Hilali A, Rhinane H, Baidder L, El Arabi H, et al. Application of remote sensing in geological mapping, case study Al Maghrabah area – Hajjah region, Yemen. In: ISPRS Annals of the Photogrammetry, Remote Sensing and Spatial Information Sciences. Safranbolu, Karabuk, Turkey; 2017. p. 63–71.

[45] Sheikhrahimi A, Pour AB, Pradhan B, Zoheir B. Mapping hydrothermal alteration zones and lineaments associated with orogenic gold mineralization using ASTER data: A case study from the Sanandaj-Sirjan Zone, Iran. Adv Sp Res. 2019;63(10): 3315–3332.

[46] Pour AB, Park Y, Crispini L, Läufer A, Hong JK, Park TS, et al. Mapping Listvenite Occurrences in the Damage Zones of Northern Victoria Land, Antarctica Using ASTER Satellite Remote Sensing Data. Remote Sens. 2019;11(12):1408.

[47] Chattoraj SL, Prasad G, Sharma RU, Champati Ray PK, Van der Meer FD, Guha A, et al. Integration of remote sensing, gravity and geochemical data for exploration of Cu-mineralization in Alwar basin, Rajasthan, India. Int J Appl Earth Obs Geoinf. 2020;91:102162 (1-12).

[48] Sekandari M, Masoumi I, Pour AB, Muslim AM, Rahmani O, Hashim M, et al. Application of Landsat-8, Sentinel-2, ASTER and WorldView-3 Spectral Imagery for Exploration of Carbonate-Hosted Pb-Zn Deposits in the Central Iranian Terrane (CIT). Remote Sens. 2020;12(8):1239 (1-33).

[49] Van der Meer FD. Imaging spectrometry for geological remote sensing. Netherlands J Geosci. 1998;77 (2):137–151.

[50] Thompson AJB, Hauff PL, Robitaille AJ. Alteration mapping in exploration; application of short-wave infrared SWIR spectroscopy. SEG Newsl. 1999;39:16–27.

[51] Thompson AJB, Hauff PL, Robitaille AJ. Alteration Mapping in Exploration: Application of Short-Wave Infrared (SWIR) Spectroscopy. In: Bedell R, Crósta AP, Grunsky E, editors. Remote Sensing and Spectral Geology. McLean, Va: Society of Economic Geologists; 2009.

[52] Jain R, Sharma RU. Mapping of Mineral Zones using the Spectral Feature Fitting Method in Jahazpur belt, Rajasthan, India. Int Res J Eng Technol. 2018;5(1):562–567.

[53] Chang CW, Laird DA, Mausbach MJ, Hurburgh CR. Near-infrared reflectance spectroscopy - Principal components regression analyses of soil properties. Soil Sci Soc Am J. 2001;65(2):480–490.

[54] Ninomiya Y, Fu B, Cudahy TJ. Detecting lithology with advanced spaceborne thermal emission and reflection radiometer (ASTER) multispectral thermal infrared "radiance-at-sensor" data. Remote Sens Environ. 2005;99(1–2):127–139.

[55] Ninomiya Y, Fu B. Regional Lithological Mapping Using ASTER-TIR Data: Case Study for the Tibetan Plateau and the Surrounding Area. Geosciences. 2016;6:39.

[56] Rockwell BW, Hofstra AF. Identification of quartz and carbonate minerals across northern Nevada using ASTER thermal infrared emissivity data- implications for geologic mapping and mineral resource investigations in well-studied and frontier areas. Geosphere. 2008;4(1):218–246.

[57] Rani K, Guha A, Pal SK, Vinod Kumar K. Comparative analysis of potentials of ASTER thermal infrared band derived emissivity composite, radiance composite and emissivity-temperature composite in geological mapping of Proterozoic rocks in parts Banswara, Rajasthan. J Indian Soc Remote Sens. 2018;46(5):771–782.

[58] Jain R, Bhu H, Purohit R. Application of Thermal Remote Sensing technique for mapping of ultramafic, carbonate and siliceous rocks using ASTER data in Southern Rajasthan, India. Curr Sci. 2020;119(6):954–961.

[59] Rajendran S, Hersi OS, Al-Harthy A, Al-Wardi M, El-Ghali MA, Al-Abri AH. Capability of Advanced Spaceborne Thermal Emission and Reflection Radiometer (ASTER) on discrimination of carbonates and associated rocks and mineral identification of eastern mountain region (Saih Hatat window) of Sultanate of Oman. Carbonates and Evaporites. 2011;26(4):351–364.

[60] Rajendran S, Nasir S. ASTER spectral sensitivity of carbonate rocks — study in Sultanate of Oman. Adv Sp Res. 2014;53(4):656–673.

[61] Pour AB, Park TYS, Park Y, Hong JK, Zoheir B, Pradhan B, et al. Application of Multi-Sensor Satellite Data for Exploration of Zn–Pb Sulfide Mineralization in the Franklinian Basin, North Greenland. Remote Sens. 2018;10 (8):1186.

[62] Yao K, Pradhan B, Idrees MO. Identification of Rocks and Their Quartz Content in Gua Musang Goldfield Using Advanced Spaceborne Thermal Emission and Reflection Radiometer Imagery. Jung HS, editor. J Sensors. 2017;2017:6794095.

[63] El Janati M, Soulaimani A, Admou H, Youbi M, Hafid A, Hefferan K. Application of ASTER remote sensing data to geological mapping of basement domains in arid regions: a case study from the Central Anti-Atlas, Iguerda inlier, Morocco. Arab J Geosci. 2014;7(6):2407–2422.

[64] Guha A, Chatterjee S, Oommen T, Vinod Kumar K, Roy SK. Synergistic use of ASTER, L-band ALOS PALSAR, and Hyperspectral AVIRIS-NG data for exploration of lode type gold deposit - A study in Hutti Maski Schist Belt, India. Ore Geol Rev. 2021;128:103818.

[65] Guha A, Chattoraj SL, Chatterjee S, Vinod Kumar K, Rao PVN, Bhaumik AK. Reflectance spectroscopy-guided broadband spectral derivative approach to detect glauconite-rich zones in fossiliferous limestone, Kachchh region, Gujarat, India. Ore Geol Rev. 2020;127:103825.

[66] Pour AB, Hashim M. ASTER, ALI and Hyperion sensors data for lithological mapping and ore minerals exploration. Springer Plus. 2014;3:130.

[67] Asadzadeh S, de Souza Filho CR. A review on spectral processing methods for geological remote sensing. International Journal of Applied Earth Observation and Geoinformation. 2016.

[68] Abbaszadeh M, Hezarkhani A. Enhancement of hydrothermal alteration zones using the spectral feature fitting method in Rabor area, Kerman, Iran. Arab J Geosci. 2013;6: 1957–1964.

[69] Goodarzi Mehr S, Ahadnejad V, Abbaspour RA, Hamzeh M. Using the mixture-tuned matched filtering method for lithological mapping with Landsat TM5 images. Int J Remote Sens. 2013;34(24):8803–8816.

[70] Zadeh MH, Tangestani MH, Roldan FV, Yusta I. Mineral exploration and alteration zone mapping using mixture tuned matched filtering approach on ASTER data at the central part of dehaj-sarduiyeh copper belt, SE

Iran. IEEE J Sel Top Appl Earth Obs Remote Sens. 2014;7(1):284–289.

[71] Porwal A, Carranza EJM, Hale M. A Hybrid Neuro-Fuzzy Model for Mineral Potential Mapping. Math Geol. 2004;36 (7):803–826.

[72] Gupta SN, Arora YK, Mathur RK, Iqballuddin, Prasad B, Sahai TN, et al. The Precambrian Geology of the Aravalli region, Southern Rajasthan & North-eastern Gujarat. Mem Geol Surv India. 1997;123:1–262.

[73] Roy AB, Jakhar SR. Geology of Rajasthan (Northwest India): Precambrian to Recent. Jodhpur: Scientific Publishers (India); 2002. 421 p.

[74] GSI. Geology and Mineral Resources of Rajasthan. 3rd ed. Kolkata, India: Geological Survey of India; 2011. 130pp.

[75] Sinha-Roy S, Malhotra G, Mohanty M. Geology of Rajasthan. Bangalore: Geological Society of India; 1998. 1-275 p.

[76] Gupta SN, Arora YK, Mathur RK, Iqballuddin, Prasad B, Sahai TN, et al. Lithostratigraphic map of Aravalli region, southern Rajasthan & northern Gujarat. Hyderabad: Geological Survey of India; 1980.

[77] Heron AM. Geology of the Central Rajasthan. Mem Geol Surv India. 1953; 79:1–389.

[78] Bhattacharyya S, Dutt K, Sarkar SS. Detailed Study of Mangalwar Complex. Abstracts of Progress reports: 1993-93. Rec Geol Surv India. 1995;127(7):1–3.

[79] Mathur RK. Systematic geological mapping in parts of Udaipur district, Rajasthan. Calcutta, India; 1964.

[80] Poddar BC, Mathur RK. A note on the repetitious sequence of greywacke–slate–phyllite in the Aravalli System around Udaipur, Rajasthan. Bull Geol Soc India. 1965;2(2):192–194.

[81] Straczek JA, Srikantan B. The Geology of the Zawar Lead–Zinc Area, Rajasthan, India. Mem Geol Surv India. 1966;92:1–85.

[82] Mookherjee A. Geology of the Zawar Lead-Zinc Mine, Rajasthan, India. Econ Geol. 1964;59(4):656–677.

[83] Poddar BC. Lead-Zinc mineralization in the Zawar Belt, India - Discussion. Econ Geol. 1965;60(3):636–638.

[84] Singh NN. Tectonic and stratigraphic framework of the lead-zinc sulphide mineralisation at Zawarmala, District Udaipur, Rajasthan. J Geol Soc India. 1988;31(6):546–564.

[85] Roy AB. Geometry and evolution of superposed folding in the Zawar lead-zinc mineralised belt, Rajasthan. Proc Indian Acad Sci (Earth Planet Sci. 1995; 104(3):349–71.

[86] Roy AB, Jain AK. Polyphase deformation in the Pb-Zn bearing Precambrian rocks of Zawarmala, Udaipur district, southern Rajasthan. Q J Geol Min Metall Soc India. 1974;46:81–86.

[87] Bhu H, Sarkar A, Purohit R, Banerjee A. Characterization of fluid involved in ultramafic rocks along the Rakhabdev Lineament from southern Rajasthan, northwest India. Curr Sci. 2006;91(9):1251–1256.

[88] Purohit R, Bhu H, Sarkar A, Ram J. Evolution of the ultramafic rocks of the Rakhabdev and Jharol belts in southeastern Rajasthan, India: New evidences from imagery mapping, petro-minerological and OH stable isotope studies. J Geol Soc India. 2015;85 (3):331–338.

[89] Ram J. Tectonism along the Rakhabdev Lineament as Exemplified by Structural and Crustal Deformation

Studies. Mohanlal Sukhadia University, Udaipur; 2014.

[90] Sarkar DP, Ando JI, Das K, Chattopadhyay A, Ghosh G, Shimizu K, et al. Serpentinite enigma of the Rakhabdev lineament in western India: Origin, deformation characterization and tectonic implications. J Mineral Petrol Sci. 2020;115(2):216–226.

[91] Chattopadhyay A, Gangopadhyay S. Petrological Studies of the Ultramafics rocks of the Rajasthan. Geol Surv India, Spec Publ. 1984;12:17–24.

[92] USGS. AST_L1T v003 [Internet]. LPDAAC. 2019 [cited 2020 Jan 13]. Available from: https://lpdaac.usgs.gov/products/ast_l1tv003/

[93] Iwasaki A, Tonooka H. Validation of a Crosstalk Correction Algorithm for ASTER/SWIR. IEEE Trans Geosci Remote Sens. 2005;43(12):2747–2751.

[94] Mars JC, Rowan LC. Spectral assessment of new ASTER SWIR surface reflectance data products for spectroscopic mapping of rocks and minerals. Remote Sens Environ. 2010; 114(9):2011–2025.

[95] Bernstein LS, Jin X, Gregor B, Adler-Golden SM. The Quick Atmospheric Correction (QUAC) Code: Algorithm Description and Recent Upgrades. SPIE Opt Eng. 2012;51(11):111719.

[96] Bernstein LS, Adler-Golden SM, Sundberg RL, Levine RY, Perkins TC, Berk A, et al. Validation of the QUick atmospheric correction (QUAC) algorithm for VNIR-SWIR multi- and hyperspectral imagery. In: Shen SS, Lewis PE, editors. Proceedings of SPIE 5806, Algorithms and Technologies for Multispectral, Hyperspectral, and Ultraspectral Imagery XI. SPIE; 2005. p. 668–678.

[97] Bernstein LS, Adler-Golden SM, Sundberg RL, Levine RY, Perkins TC, Berk A, et al. A New Method for Atmospheric Correction and Aerosol Optical Property Retrieval for VIS-SWIR Multi- and Hyperspectral Imaging Sensors: Quick Atmospheric Correction. In: Green RO, editor. Proceedings of 13th JPL Airborne Earth Science Workshop. Pasadena, CA: Jet Propulsion Laboratory, California Institute of Technology; 2004. p. 9–20.

[98] Saini V, Tiwari RK, Gupta RP. Comparison of FLAASH and QUAC atmospheric correction methods for Resourcesat-2 LISS-IV data. In: Proceedings of SPIE 9881, In Earth observing missions and sensors: Development, implementation, and characterization IV. New Delhi, India: SPIE; 2016.

[99] Zhu S, Lei B, Wu Y. Retrieval of Hyperspectral Surface Reflectance Based on Machine Learning. Remote Sens. 2018;10(2):323.

[100] Lentilucci EJ, Adler-Golden SM. Atmospheric Compensation of Hyperspectral Data: An Overview and Review of In-Scene and Physics-Based Approaches. IEEE Geosci Remote Sens Mag. 2019;7(2):31–50.

[101] Ninomiya Y, Fu B. Thermal infrared multispectral remote sensing of lithology and mineralogy based on spectral properties of materials. Ore Geol Rev. 2019;108:54–72.

[102] Jain R. Geological Studies using the Imaging Spectroscopy and Polarimetric Synthetic Aperture Radar (SAR) data in Zawar (Distt: Udaipur). Mohanlal Sukhadia University, Udaipur; 2021.

[103] Van der Meer FD. Analysis of spectral absorption features in Hyperspectral Imagery. Int J Appl Earth Obs Geoinf. 2004;5(1):55–68.

[104] Wang JN, Zheng LF. The Spectral Absorption Identification Model and Mineral Mapping by Imaging

Spectrometer Data. Remote Sens Environ China. 1996;1:20–31.

[105] Mars JC, Rowan LC. Regional mapping of phyllic- and argillic-altered rocks in the Zagros magmatic arc, Iran, using Advanced Spaceborne Thermal Emission and Reflection Radiometer (ASTER) data and logical operator algorithms. Geosphere. 2006;2(3): 161–186.

[106] Hewson RD, Cudahy TJ, Mizuhiko S, Ueda K, Mauger AJ. Seamless geological map generation using ASTER in the Broken Hill-Curnamona province of Australia. Remote Sens Environ. 2005;99(1–2): 159–172.

[107] Cudahy TJ, Hewson R, Buchanan A, Maruyama Y, Mauger Creasey J, Veridan. A generation of geological and regolith maps derived from multispectral VNIR-SWIR-TIR ASTER satellite data. In: Proceedings of the Fourteenth International Conference on Applied Geologic Remote Sensing. USA; 2000. p. 159.

[108] Crosta AP, De Souza Filho CR, Azevedo F, Brodie C. Targeting key alteration minerals in epithermal deposits in Patagonia, Argentina, using ASTER imagery and principal component analysis. Int J Remote Sens. 2003;24(21):4233–4240.

[109] Yajima T, Yamaguchi Y. Geological mapping of the Francistown area in northeastern Botswana by surface temperature and spectral emissivity information derived from Advanced Spaceborne Thermal Emission and Reflection Radiometer (ASTER) thermal infrared data. Ore Geol Rev. 2013;53:134–144.

[110] Son YS, Kang MK, Yoon WJ. Lithological and mineralogical survey of the Oyu Tolgoi region, Southeastern Gobi, Mongolia using ASTER reflectance and emissivity data. Int J Appl Earth Obs Geoinf. 2014;26: 205–216.

[111] Roy AB, Bejarniya BR. A tectonic model for the early Proterozoic Aravalli (Supergroup) rock from north of Udaipur, Rajasthan. In: Sychanthavong SPH, editor. Crustal Evolution and Orogeny. New Delhi, India: Oxford and IBH Publishing Co. Pvt. Ltd.; 1990. p. 249–273.

[112] Verma PK, Greiling RO. Tectonic evolution of the Aravalli orogen (NW India): an inverted Proterozoic rift basin? Geol Rundsch. 1995;84(4):683–696.

[113] Roy AB. Stratigraphic and tectonic framework of the Aravalli Mountain Range. In : A.B. Roy (Eds.) Precambrians of Aravalli Mountain, Rajasthan, India. Mem Geol Soc India. 1988;7:3–31.

[114] Salaj SS, Prabhakaran, Upadhyay R, Srivastav SK. Mineral abundance mapping using hyperion dataset in Udaipur, India. Geospatial World [Internet]. 2012; Available from: https://www.geospatialworld.net/article/mineral-abundance-mapping-using-hyperion-dataset-in-udaipur-india/

[115] Kumar H, Rajawat AS. Aqueous alteration mapping in Rishabdev ultramafic complex using imaging spectroscopy. Int J Appl Earth Obs Geoinf. 2020;88:102084.